ADVANCED OPTICAL MATERIALS
www.advopticalmat.de

Asymmetrically Contacted Tellurium Short-Wave Infrared Photodetector with Low Dark Current and High Sensitivity at Room Temperature

Huide Wang, Haoxin Huang, Jiajia Zha, Yunpeng Xia, Peng Yang, Yonghong Zeng, Yi Liu, Rui Cao, Bing Wang, Wei Wang, Long Zheng, Ye Chen, Qiyuan He, Xing Chen, Ke Jiang, Ja-Hon Lin, Zhe Shi, Johnny C. Ho, Han Zhang, and Chaoliang Tan**

Large dark current at room temperature has long been the major bottleneck that impedes the development of high-performance infrared photodetectors toward miniaturization and integration. Although infrared photodetectors based on layered 2D narrow bandgap semiconductors have shown admirable advantages compared with those based on conventional compounds, which typically suffer from the expensive cryogenic operation, it is still urgent to develop a simple but effective strategy to further reduce the dark current. Herein, a tellurium (Te)-based infrared photodetector is reported with specifically designed asymmetric electrical contact area. The deliberately introduced asymmetric electrical contact raises the electric field intensity difference in the Te channel near the drain and the source electrodes, resulting in the spontaneous asymmetric carrier diffusion under global infrared light illumination under zero bias. Specifically, the Te-based photodetector presents promising detector performance at room temperature including a low dark current of ≈1 nA, an ultrahigh photocurrent/dark current ratio of 1.57×10^4, a high specific detectivity (*D) of 3.24×10^9 Jones, and a relatively fast response speed of ≈720 µs at zero bias. The results prove that the simple design of asymmetric electrical contact areas can provide a promising solution to high-performance 2D semiconductor-based infrared photodetectors working at room temperature.**

1. Introduction

Infrared photodetection is indispensable in optical communication, spectral analysis, biomedicine, and remote sensing.[1–3] Layered 2D materials are expected to be the promising building blocks for next-generation infrared photodetection system by virtue of their relatively simple preparation process, strong light-matter interaction, high-quality surface without dangling bonds, facile heterostructure integration, and high compatibility with complementary metal-oxide-semiconductor (COMS) process.[4–6] The commonly used layered materials for infrared photodetection include elemental materials like graphene (near zero bandgap),[7,8] black phosphorus (BP) (bandgap of ≈0.3–2.0 eV),[6,9] tellurium (Te) (bandgap of ≈0.3–1.0 eV),[10,11] and noble metal dichalcogenides like few-layer platinum diselenide ($PtSe_2$) (bandgap of ≈0–1.2 eV)[12,13] and palladium diselenide ($PdSe_2$) (bandgap of ≈0–1.3 eV).[14–16] Among them, crystalline 2D Te is heavily studied since it not only

H. Wang, J. Zha, W. Wang, Q. He, J. C. Ho
Department of Materials Science and Engineering
City University of Hong Kong
Hong Kong SAR 9990777, China

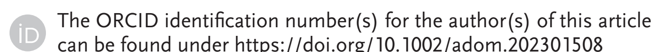
The ORCID identification number(s) for the author(s) of this article can be found under https://doi.org/10.1002/adom.202301508

© 2023 The Authors. Advanced Optical Materials published by Wiley-VCH GmbH. This is an open access article under the terms of the Creative Commons Attribution-NonCommercial License, which permits use, distribution and reproduction in any medium, provided the original work is properly cited and is not used for commercial purposes.

DOI: 10.1002/adom.202301508

H. Wang, Y. Zeng, Y. Liu, R. Cao, B. Wang, H. Zhang
International Collaborative Laboratory of 2D Materials for Optoelectronics Science and Technology
Interdisciplinary Center of High Magnetic Field Physics of Shenzhen University
College of Physics and Optoelectronic Engineering
Shenzhen University
Shenzhen 518060, China
E-mail: hzhang@szu.edu.cn

H. Wang, H. Huang, Y. Xia
Department of Electrical Engineering
City University of Hong Kong
Hong Kong SAR 999077, China

P. Yang
College of Integrated Circuits and Optoelectronic Chips
Shenzhen Technology University
Shenzhen 518118, China

possesses suitable bandgap and high mobility of 1755 cm^2 V^{-1} s^{-1} (room temperature), but is also highly environmentally adaptable together with low-cost manufacturing strategies.[17–21] The attractive potential of Te for short-wave infrared (SWIR) photodetection, large-scale circuits, and future smart signal processing systems has also been demonstrated in our earlier studies.[10,22,23] However, high noise and relatively poor specific detectivity (D^*) is still limited by the large dark current in Te-based photodetectors originating from its narrow bandgap.[10,11,24] That is, even when optical absorption of Te is significantly enhanced by optical cavity substrates consisting of Au/Al_2O_3, the D^* is only 2 × 10^9 Jones. To improve this situation, we first successfully prepared Se_xTe_{1-x} alloy films with tunable bandgaps by alloying Te with large bandgap Se for the fabrication of high-performance SWIR photodetectors.[25,26] The infrared photodetector fabricated from the Se_xTe_{1-x} thin film on an optical cavity substrate exhibits a room-temperature detectivity of 6.5 × 10^{10} Jones at 1.55 µm and the whole focal plane arrays (FPAs) shows great SWIR imaging potential with excellent pixel uniformity. However, there are rich defects and grain boundaries within the evaporated polycrystalline Se_xTe_{1-x} thin films, leading to the relatively large dark current. Therefore, it still remains a daunting challenge to effectively suppress the dark current for the construction of high-performance infrared photodetectors based on layered 2D semiconductors.

Until now, several effective strategies have been developed to improve the situation. i) The first method is to introduce electrostatic doping to reduce the dark current via constructing phototransistors.[9,27] ii) The second method leverages the built-in potential in the constructed p-n heterojunctions.[28–33] Due to the existence of depletion region, the device will exhibit a low dark current at reverse bias. iii) To further improve the energy efficiency in method (i), the third method is to substitute the oxide dielectric in phototransistor with ferroelectric ones, where the permanent electrical polarizations in ferroelectric layer can help suppress the dark current in channel.[34–36] iv) The fourth method is to construct nBn or pBp unipolar barrier heterojunction by elaborately adding an additional barrier layer, in this way, the dark current related to the movement of majority carriers can be significantly depleted without the suppression of photocurrent. Taking the nBn structure as an example, the barrier in conduction band can effectively block the movement of majority carriers in the absorption layer, so that the diffusion current, surface leakage current, Shockley–Read–Hall (SRH) recombination current and Auger recombination current can be effectively inhibited, and finally an ultralow dark current (e.g., 15 pA) can be obtained.[37] v) The fifth method is to use asymmetric electrical contact to obtain self-powered photoresponse, where the dark current can be reduced to zero theoretically for the lack of external power supply. Asymmetric electrical contact can be realized by electrodes with asymmetric work function,[38–40] asymmetric van der Waals contacts,[41–43] asymmetric channel widths,[44,45] etc. Compared with other strategies, this method is much more convenient and energy efficient.

In this work, we report a simple asymmetric electrical contact strategy for the fabrication of high-performance Te infrared photodetector with low dark current and high sensitivity at room temperature. In this strategy, the contact areas between channel material (Te) and drain/source electrodes were deliberately designed to be asymmetric. Then, the carrier diffusion in Te nanobelt above the drain and source electrodes to the channel part were rearranged, leading to the asymmetric band bending in the channel. Therefore, this device exhibits fascinating infrared photoresponse at zero bias, where the observed dark current of the device was in a very low level due to the absence of external bias. The working mechanism of the device was then systematically investigated via scanning photocurrent mapping (SPCM) and Kelvin probe force microscope (KPFM). The attractive room-temperature photoresponse obtained in this device toward infrared (1550 nm) light at zero bias includes the low dark current of ≈1 nA, the ultrahigh photocurrent/dark current ratio of 1.57 × 10^4, the high responsivity (R) of 26.1 A W^{-1}, the high specific detectivity (D^*) of 3.24 × 10^9 Jones, and the relatively fast response speed of ≈720 µs. The D^* of our device is not only higher than that of the previously reported Te-based devices without an optical cavity substrate,[46] but also slightly higher than that of Te-based devices with an optical cavity substrate,[10] which uncovers the great potential of this simple design strategy in the field of high-performance infrared photodetection.

2. Results and Discussion

The Te nanobelts/nanosheets were grown by a typical chemical vapor deposition (CVD) using TeO_2 as the precursor and H_2 as the reducing gas (see the Experimental Section for details). The optical microscope images in Figure S1 (Supporting Information) show the CVD-grown Te nanobelts/nanosheets along with small portion of nanowires. Their thicknesses of Te nanobelts/nanosheets range from 100 to 1000 nm, which were characterized by atomic force microscope (AFM) (Figure S2, Supporting Information). **Figure 1**a shows a transmission electron microscope (TEM) image of a typical Te nanobelt. The

L. Zheng, Y. Chen
Department of Chemistry
The Chinese University of Hong Kong
Hong Kong SAR 999077, China
X. Chen
College of Mathematics and Physics
Chengdu University of Technology
Chengdu 610041, China
K. Jiang
State Key Laboratory of Luminescence and Applications
Changchun Institute of Optics
Fine Mechanics and Physics
Chinese Academy of Sciences
Changchun 130033, China
J.-H. Lin
Advanced Nanophotonics Technology Laboratory
Department of Electro-Optical Engineering
National Taipei University of Technology
Taipei 10608, Taiwan
Z. Shi
School of Physics & New Energy
Xuzhou University of Technology
Xuzhou 221018, China
C. Tan
Department of Electrical and Electronic Engineering
The University of Hong Kong
Pokfulam Road, Hong Kong SAR 999077, China
E-mail: cltan@hku.hk

© 2023 The Authors. Advanced Optical Materials published by Wiley-VCH GmbH

21951071, 2023, 23, Downloaded from https://onlinelibrary.wiley.com/doi/10.1002/adom.202301508 by City Universitaet Of Hong Kong, Wiley Online Library on [10/12/2023]. See the Terms and Conditions (https://onlinelibrary.wiley.com/terms-and-conditions) on Wiley Online Library for rules of use; OA articles are governed by the applicable Creative Commons License

21951071, 2023, 23, Downloaded from https://onlinelibrary.wiley.com/doi/10.1002/adom.202301508 by City Universitaet Of Hong Kong, Wiley Online Library on [10/12/2023]. See the Terms and Conditions (https://onlinelibrary.wiley.com/terms-and-conditions) on Wiley Online Library for rules of use; OA articles are governed by the applicable Creative Commons License

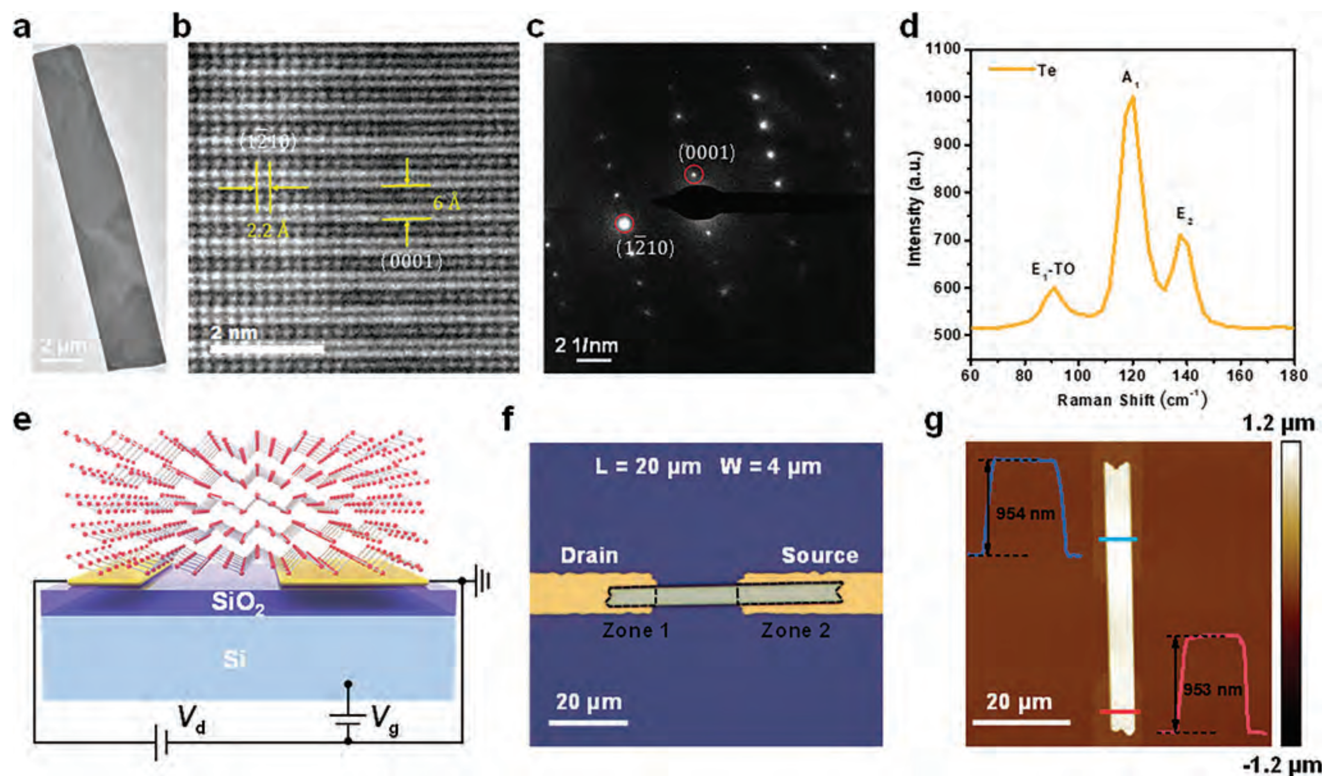

Figure 1. Preparation and characterization of Te nanobelts and Te photodetector. a) TEM image, b) corresponding HR-TEM image, and c) SAED pattern of a typical Te nanobelt. d) The Raman spectrum of the Te nanobelt. e) Schematic illustration of the Te photodetector with asymmetric electrical contact area. f) The optical image of the Te device. g) The AFM image of the Te device. Inset depicts the height profiles of Te above the drain/source ends.

corresponding high-resolution TEM (HR-TEM) image is also provided (Figure 1b), showing continuous lattices of the Te nanobelt with interplanar spacings of 2.2 and 6.0 Å, which can be assigned to the (1$\bar{2}$10) and *(0001)* planes of Te crystal (Figure 1b). The corresponding selected area electron diffraction (SAED) pattern is presented in Figure 1c. Bright rectangular diffraction spots are shown in the corresponding SAED pattern, and the two spots closest to the diffraction center manifest the (1$\bar{2}$10) and (0001) planes of the Te crystal (Figure 1c). Both the HR-TEM and SAED pattern confirm that the Te nanobelts synthesized by CVD method are single-crystalline.[10,17,19] Three Raman peaks at 91 cm^{-1} (E_1 transverse (TO) phonon mode), 119 cm^{-1} (A_1 mode) and 139 cm^{-1} (E_2 mode) are observed from the Raman spectrum (Figure 1d). It is worth pointing out that the longitudinal (LO) phonon mode was not observed, which is consistent with the Raman features of thick Te samples reported elsewhere.[17,19,47] In the following experiments, the relatively thick Te nanobelts were selected for device fabrication. In order to construct devices with asymmetric electrical contact area, drain and source electrodes (10 nm Cr/70 nm Au) were first deposited on 300 nm SiO_2/p^{++}-Si substrate. Then, the Te nanobelt grown on mica substrate by CVD method was transferred onto the as-prepared electrodes by dry transfer technique.[48–50] The schematic diagram and optical image of the Te-based photodetector are shown in Figure 1e,f, where the contact area between Te nanobelt and electrodes in the drain end (Zone 1) was smaller than that in the source end (Zone 2). The channel length and width of the device are 20 and 4 µm, respectively. It can be concluded that the thickness of Te nanobelts in the device is very uniform from AFM results, and the thickness of the Te nanobelt above drain and source electrodes are very close (953/954 nm) (Figure 1g).

After the device preparation, the electrical properties of the devices at ambient condition were studied. The almost symmetrical output characteristics of the devices indicate the asymmetry of the device is not obvious in the dark (**Figure 2**a; Figure S3, Supporting Information). The linear relationship between current and voltage indicates that Te forms good Ohmic contact with Au electrodes. The transfer curves of the device exhibited in Figure 2b confirm the hole-dominated transport characteristics of the Te samples. The field-effect hole mobility (μ_{FE}) of the Te FET can be calculated from the following formula:[51,52]

$$\mu_{\mathrm{FE}} = \frac{g_{\mathrm{m}} L}{W C_{\mathrm{g}} V_{\mathrm{ds}}} \tag{1}$$

where g_m, L, W, and C_g are the transconductance, channel length, channel width, and SiO_2 capacitance, respectively. The calculated room-temperature μ_{FE} as a function of the gate voltage in the Te device are shown in Figure 2c, which showed a high hole mobility under different V_d with little variation. Specifically, the extracted peak hole mobilities of the device at V_d = 0.01 V, 0.02 V, 0.05 V, and 0.1 V were as high as 757.0, 744.9, 748.9, and 754.2 $cm^2\ V^{-1}s^{-1}$, respectively. The high hole mobility further demonstrated the high quality of Te nanobelts.

The infrared photoresponse of the Te photodetector is further studied and summarized in Figure 2d–i. The spot area of the

 © 2023 The Authors. Advanced Optical Materials published by Wiley-VCH GmbH

21951071, 2023, 23, Downloaded from https://onlinelibrary.wiley.com/doi/10.1002/adom.202301508 by City Universitat Of Hong Kong, Wiley Online Library on [10/12/2023]. See the Terms and Conditions (https://onlinelibrary.wiley.com/terms-and-conditions) on Wiley Online Library for rules of use; OA articles are governed by the applicable Creative Commons License

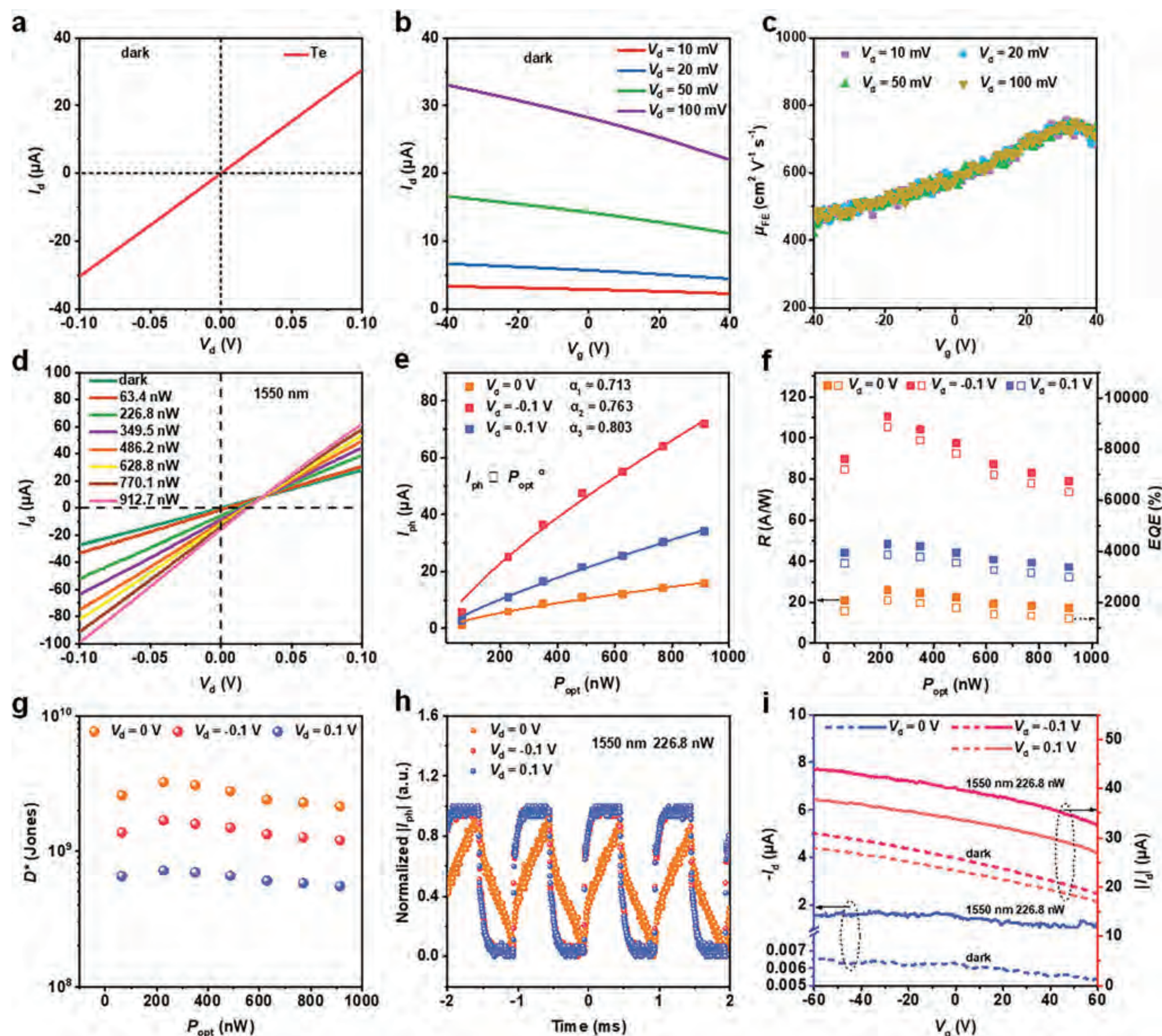

Figure 2. Electrical properties and photoresponse of Te photodetector. a) Output curve and b) transfer curves of the Te photodetector. c) The calculated field-effect hole mobilities. d) Output curves at different P_{opt}. e–g) The P_{opt} dependent scatter plots of e) I_{ph}, f) R and EQE, g) D^*. h) Normalized time-resolved photocurrent curves. i) Transfer curves under dark and illumination.

laser beam used in the test is significantly greater than the area of the device, thus the global illumination across the entire device is considered as uniform. The self-powered asymmetric output characteristics under illumination of different laser power (P_{opt}) is presented in Figure 2d. Figure S4a (Supporting Information) provides the optical power dependent photocurrent as a function of V_d. The laser power dependent photocurrent at $V_d = -0.1$ V, 0 V, and 0.1 V is depicted by the scatter diagram in Figure 2e. It can be found that the photocurrent increases almost linearly with the optical power. Furthermore, the loss of photogenerated carriers can be evaluated by the power law:[53–55]

$$I_{ph} \propto P_{opt}^{\alpha} \quad (2)$$

where, I_{ph}, P_{opt}, α are the photocurrent, optical power and a constant to be fitted, respectively. The α of device are 0.763, 0.713, and 0.803 at $V_d = -0.1$ V, 0 V, and 0.1 V, respectively. The greatest photogenerated carrier loss is observed at $V_d = 0$ V, which can be attributed to the lack of external electric field at zero bias. In addition, R (Figure 2f), external quantum efficiency (EQE) (Figure 2f) and D^* (Figure 2g) at different V_d can be calculated according to Note S1 (Supporting Information). According to Figure 2f,g, the peak values of R, EQE, D^* of the device are obtained at the optical power of ≈226.8 nW under different bias. When V_d is −0.1, 0, or 0.1 V, the calculated R is as high as 110.6, 26.1, or 48.4 A W^{-1}, together with high EQE of 8862.2%, 2090.9%, or 3883.8%, respectively. Although R and EQE of the device at zero bias are smaller than those at non-zero bias, the dark current measured

© 2023 The Authors. Advanced Optical Materials published by Wiley-VCH GmbH

ADVANCED OPTICAL MATERIALS
www.advopticalmat.de

at non-zero bias is in the level of μA. On the other hand, the dark current of the device at zero bias should be theoretically zero, holding a great promise to achieve high D^*. In measuring the time-resolved photoresponse at zero bias (Figure S4b, Supporting Information) the dark current of the device is found to be non-zero (≈1 nA). The existence of non-zero dark current may be explained by the combination of asymmetric band bending caused by asymmetric electrical contact area and the incomplete equilibrium state of the device after the illumination was removed. If the dark current is the major contributor to shot noise, the calculated specific detectivity is denoted as D_0^*. According to Note S1 and Figure S4c (Supporting Information), the calculated $D_0^* = 1.30 \times 10^{12}$ Jones at $V_d = 0$ V is much higher than that at $V_d = -0.1$ V ($D_0^* = 3.34 \times 10^{10}$ Jones) and $V_d = 0.1$ V ($D_0^* = 1.46 \times 10^{10}$ Jones) ($P_{opt} = 226.8$ nW). In addition, the spectra of current noise power density (i_n^2) were carried out to more accurately demonstrate the detection capability of Te based device (Figure S16a, Supporting Information). At $V_d = 0$ V, there showed two typical noises of $1/f$ noise and generation-recombination (g-r) noise in the regions of $f < 1$ kHz and $f > 1$ kHz, respectively. In order to distinguish easily, the specific detectivity calculated by using the spectra of current noise power density was denoted as D^*. The noise equivalent power (*NEP*) and D^* can be calculated according to i_n^2, as shown in Figure S16b (Supporting Information) and Figure 2g. The calculated $D^* = 3.24 \times 10^9$ Jones at $V_d = 0$ V is also higher than that at $V_d = -0.1$ V (1.69×10^9 Jones) and $V_d = 0.1$ V (7.18×10^8 Jones) ($P_{opt} = 226.8$ nW). The I_{ph}/I_{dark} ratio versus P_{opt} is further calculated as shown in Figure S4d (Supporting Information) and the peak I_{ph}/I_{dark} ratio under different bias voltages is calculated to be 2.6, 15782.1, and 1.2 under $V_d = -0.1$ V, 0 V or 0.1 V ($P_{opt} = 912.7$ nW), respectively. The obviously higher I_{ph}/I_{dark} ratio at $V_d = 0$ V further highlights the significance of the asymmetrical contact design strategy. Our Te device also shows a relatively fast response speed in μs level (Figure 2h; Figure S4e, Supporting Information). Here the rise (fall) time was denoted as the time required for the photocurrent to change from 10% (90%) to 90% (10%) of its stable value. At $V_d = -0.1$ V, 0 V or 0.1 V under $P_{opt} = 226.8$ nW, the extracted rise time/fall time of the device can reach ≈62 μs/≈100 μs, ≈720 μs/≈1.16 ms or ≈62 μs/≈100 μs, respectively. The gate voltage dependent photoresponse curves are also recorded as shown in Figure 2i and Figure S4f (Supporting Information), and the photocurrent of the device can only be regulated in a limited range. The reason is that the Te channel is relatively thick.[22,56]

SPCM and KPFM were further employed to uncover the working mechanism behind the Te device with asymmetric contact. During the SPCM measurements, the drain, source, and gate electrodes were arranged as indicated in Figure 1e. The gate voltage was grounded and the spot diameter of the focused laser is ≈1 μm. The SPCM results at $V_d = 0$ V are presented in **Figure 3**a and Figure S6a (Supporting Information) and it confirms that the photocurrent can only be generated in Te nanobelt, and the dark current of the device are denoted by the data for current at positions where Te nanobelt is absent. Note that the dark current obtained here is slightly larger than their actual value due to the stray light from the focused laser. The following three key information can be extracted from the SPCM results: i) When the laser irradiates on the Te nanobelt near the drain electrode, the negative I_d is obtained, while the laser irradiates on the Te nanobelt near the source electrode, the positive I_d is obtained. ii) The absolute value of the negative currents is higher than the positive current. iii) The position in the Te channel with the lowest absolute value of I_d is to the right of the channel's center. The SPCM results at $V_d = -0.1$ V are shown in Figure 3b and Figure S6b (Supporting Information). It can be seen that the I_d are negative, and the photocurrents are mainly generated in the Te nanobelt on the drain electrode and the Te channel, and the maximum photocurrent is located at the boundary between the drain electrode and the Te channel. The SPCM results at $V_d = 0.1$ V are shown in Figure 3c and Figure S6c (Supporting Information). It can be seen that the I_d are positive, and the photocurrents are mainly generated in the Te nanobelt on the source electrode and the Te channel, and the maximum photocurrent is located at the boundary between the source electrode and the Te channel. The SPCM results at $V_d = 0$ V, −0.2 V, and 0.2 V present the same trend (Figure S7, Supporting Information).

The KPFM test carried out in the dark provides details on the surface potential of Te device (Figure 3d,e). The results convey a lower surface potential at the area close to the channel center than the areas close to the drain/source electrodes. In addition, the surface potential difference (SPD) between Te on the drain (source) electrode far away from the Te channel and Au (obtained at the position of solid line D_2 (S_2) in Figure 3d) is larger than that between Te on the drain (source) electrode near the Te channel and Au (obtained at the position of solid line D_1 (S_1) in Figure 3d). The SPD between the Te and Au at the location of line D_1, D_2, S_1 and S_2 is ≈90, 110, ≈89, and 108 mV, respectively. These results show that there is a process of carrier diffusion in the Te above the drain electrode/source electrode into the Te channel.

According to these experimental results, the working mechanism of the Te device with asymmetric electrical contact area is further analyzed with the help of energy band diagram. For the convenience of description, the x-y-z Cartesian coordinate system of the device are first established (**Figure 4**a). Then the energy band diagram of the thick Te nanobelt was initialized according to previous reports (Figure 4b).[29] Because the Fermi level of Te differs from the work function of Au, band bending occurs at the interface between Te and the drain/source electrodes, which results in hole accumulation at the interface, while electron accumulation occurs in Te far away from the interface (Figure 4c). Low-temperature electrical transport characterization also confirmed this band bending. The test results (Figure S5, Supporting Information) show that the Schottky barrier heights (SBH) at the Te/Au interfaces are negative, suggesting that the energy band of Te at the Te/Au interfaces along z-axis direction in Figure 4c are bent upward and Ohmic contact will be formed. Then, the accumulated electrons tend to diffuse into the Te channel. It is worth noting that the diffusion capacity of the accumulated electrons in Te on the drain/source electrodes into the channel is not exactly the same as explained next (Figure 4d). Specifically, the few accumulated holes at the interface of Te and drain electrode for the small contact area, result in a weaker binding force between accumulated holes and electrons than those at source electrode. Therefore, electrons in the Te above the drain electrode are easier to diffuse into the Te channel with longer diffusion distance than electrons in the Te above the source electrode. Subsequently, the majority carrier (hole) concentration of Te above the drain electrode is greater than that of Te above the source electrode,

© 2023 The Authors. Advanced Optical Materials published by Wiley-VCH GmbH
21951071, 2023, 23, Downloaded from https://onlinelibrary.wiley.com/doi/10.1002/adom.202301508 by City Universitaet Of Hong Kong, Wiley Online Library on [10/12/2023]. See the Terms and Conditions (https://onlinelibrary.wiley.com/terms-and-conditions) on Wiley Online Library for rules of use; OA articles are governed by the applicable Creative Commons License

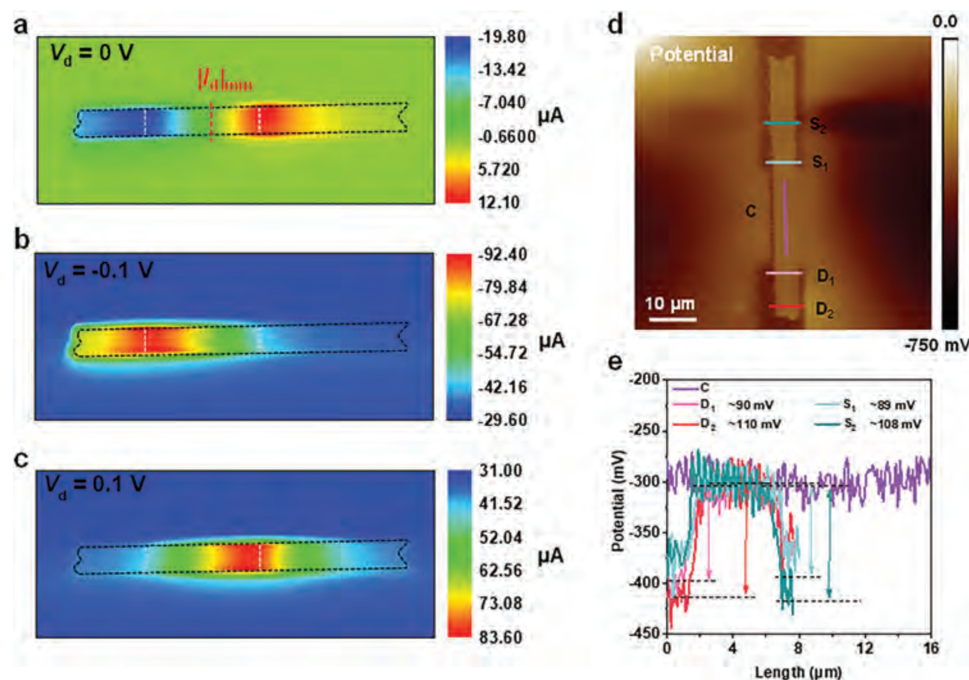

Figure 3. SPCM and KPFM results of a Te photodetector. a–c) SPCM results under 532 nm illumination with the optical power of 1 mW and the integration time of 0.2 s, at $V_d = 0$ V (a), $V_d = -0.1$ V (b), and $V_d = 0.1$ V (c), respectively. The black dashed boxes represent the boundaries of the Te nanobelt. The white dashed lines delineate the boundaries between the electrodes and Te channel. The red dashed line indicates the position in the Te channel where the absolute value of the I_d is the least. d) KPFM image of the device. e) Extracted potential curves at different position from the KPFM image (denoted by C, D_1, D_2, S_1, and S_2 in (d)).

resulting in a stronger band bending and greater electric field intensity at the Te/drain electrode interface (Figure 4e,f). However, in Te devices with symmetrical electrical contact, the diffusion capacity (Figure S10a, Supporting Information) and the degree of band bending (Figure S10b,c, Supporting Information) described above are symmetric, so symmetric Te devices can not generate photocurrent at zero bias.

Therefore, as confirmed by the SPCM results, when $V_d = 0$ V, Te above the drain electrode generates a larger photocurrent than Te above the source electrode, and the position with the smallest photocurrent in the Te channel is on the right of the channel center. When $V_d = -0.1$ V and 0.1 V, the photocurrent is mainly generated from the band bending region at Te/drain electrode interface and the Te/source electrode interface, respectively. Owing to a stronger band bending and greater electric field intensity at the Te/drain electrode interface, the measured photocurrent at $V_d = -0.1$ V is higher than that at $V_d = 0.1$ V. The Te on a small electrode has a lower surface electron concentration than the Te on a large electrode, which also results in a lower surface potential, i.e., a smaller SPD between the Te and the electrode (Figure S9, Supporting Information). So, when the device is completely covered by the laser spot, the drain and source electrodes will produce an asymmetric photocurrent or self-powered photocurrent. These analyses uncover that the asymmetric band bending caused by the asymmetric electrical contact area is responsible for the high sensitivity photodetection at zero bias observed in the device. Furthermore, the Te devices with different asymmetry ratios of electrical contact were fabricated and tested. The results show that the photoresponse at zero bias is positively correlated with the asymmetry ratio (Figure S8, Supporting Information). When the electrical contact is completely symmetric, almost no photoresponse at zero bias was observed.

To further investigate the application potential of the device, a single-pixel imaging system was demonstrated. The schematic diagram of the imaging system is shown in **Figure 5**a, where the 405 nm laser was used as the light source to irradiate the entire Te device (the spot size is ≈5 mm). Then a stepper motor is employed to move the position of the mask with the image of "SZU CityU", and the step size is set to be 0.5 mm in both X and Y directions. The spatially resolved drain-source current of the Te device in real-time is finally recorded through the computer connected to the semiconductor analyzer. The imaging results are presented in Figure 5b, where the clear image obtained at zero bias fully manifests the high stability and sensitivity of the device for imaging applications.

The polarization photoresponse of Te device was also investigated. The Te nanobelt exhibited laser polarization direction dependent optical characteristics, which is demonstrated in the angle-resolved Raman spectra and time-resolved polarized photoresponse (Figure S11, Supporting Information). The anisotropic photocurrent ratio of the Te device was ≈1.425 (Figure S12, Supporting Information), which is similar to the value reported previously.[11] These results indicate that our Te devices have the potential for further application in polarized photodetection. Asymmetric Te devices made from electrodes with asymmetric work functions are also studied with regard to their electrical and photoelectric characteristics. The Cr/Au electrode, Au electrode, and the heavily doped Si substrate were set as the

© 2023 The Authors. Advanced Optical Materials published by Wiley-VCH GmbH

21951071, 2023, 23, Downloaded from https://onlinelibrary.wiley.com/doi/10.1002/adom.202301508 by City Universitaet Of Hong Kong, Wiley Online Library on [10/12/2023]. See the Terms and Conditions (https://onlinelibrary.wiley.com/terms-and-conditions) on Wiley Online Library for rules of use; OA articles are governed by the applicable Creative Commons License

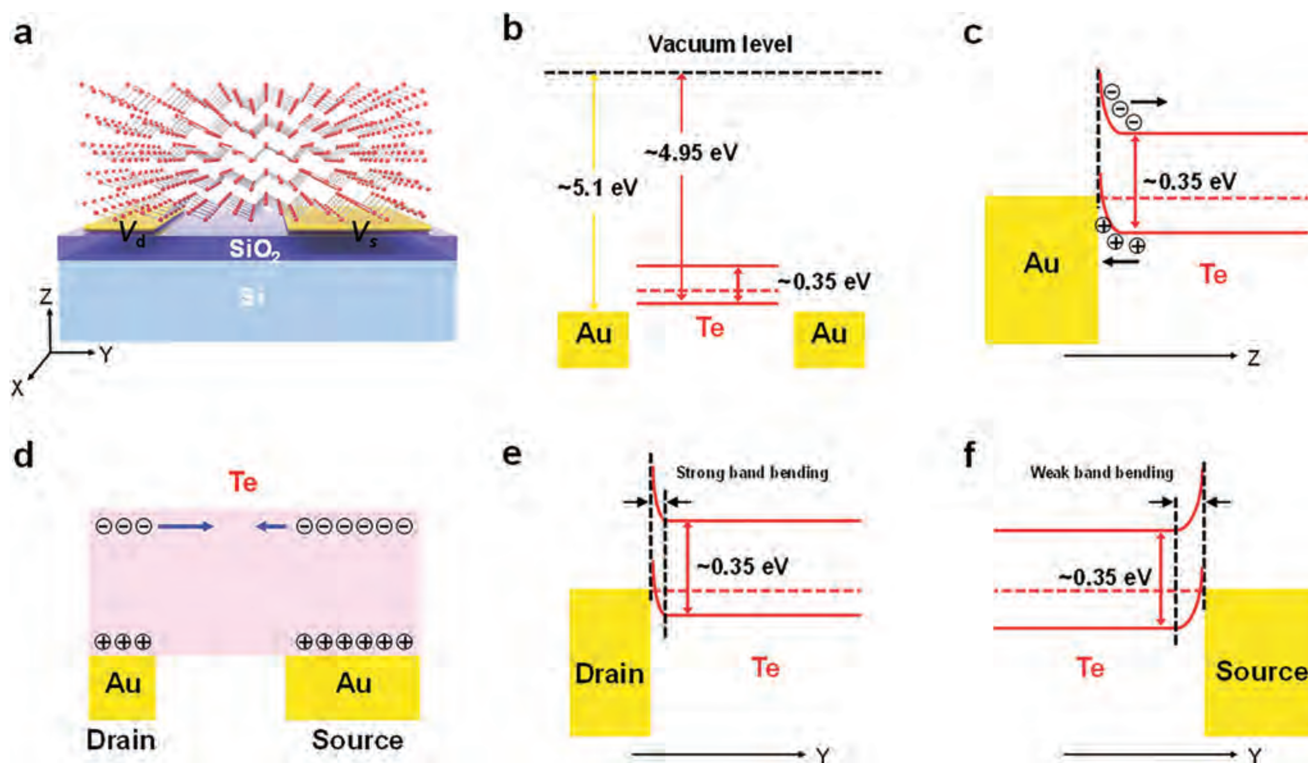

Figure 4. Mechanism analysis of asymmetrical photoresponse. a) Schematic diagram of Te device in the specified Cartesian coordinate system. b) The energy band diagram of Te before contacting the electrode. c) Band adjustment along the z axis after Te contacting the electrode. d) The schematic diagram of the movement of accumulated electrons into the Te channel. e,f) The schematic diagram of the band bending between Te and the drain electrode (e) or between Te and the source electrode (f).

drain, source, and gate electrodes, respectively (Figure S13a, Supporting Information). Obvious asymmetric electrical properties can be observed in both output (Figure S13b, Supporting Information) and transfer characteristics (Figure S13c,d, Supporting Information). The asymmetry can be attributed to the asymmetric electrodes with different work functions. And the mobilities extracted from the transfer curves at different bias are almost the same (300–400 $cm^2 V^{-1} s^{-1}$) (Figure S13e,f, Supporting Information). In the optical power dependent photoelectric characteristics (Figure S14, Supporting Information), the asymmetric photoresponse and self-powered photoresponse were observed. When P_{opt} = 11.8 nW for self-powered photoresponse, the extracted R is the highest (0.64 A W^{-1}). The small self-powered R recorded here is postulated to the larger contact barrier at the Cr/Te interface, which hinders the transport of photogenerated carriers. The gate voltage dependent electrical and photoelectric responses were also observed (Figure S15, Supporting Information). However, the device still exhibits a relatively low R of 0.72 A W^{-1} at an optimized gate voltage and $V_d = 0$ V.

3. Conclusion

In summary, we have developed a simple but effective design strategy for Te nanobelt-based infrared photodetector with low dark current and high sensitivity at room temperature. In this strategy, the device consists of the channel material and

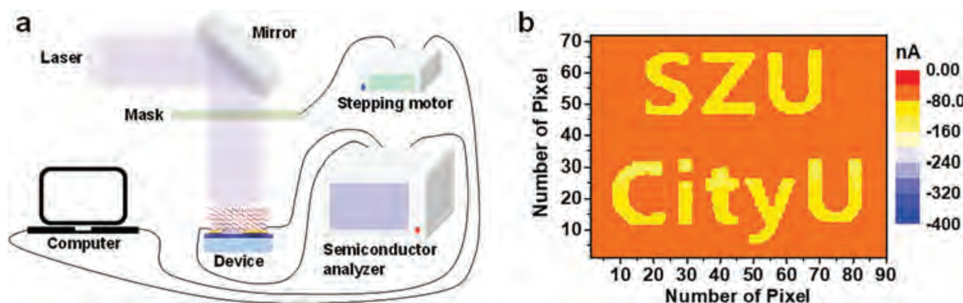

Figure 5. Single-pixel imaging at zero bias of Te photodetector. a) Schematic diagram of the single-pixel imaging system based on the asymmetric Te device. b) The drain-source current mapping of the image of "SZU CityU" under 405 nm illumination.

© 2023 The Authors. Advanced Optical Materials published by Wiley-VCH GmbH

21951071, 2023, 23, Downloaded from https://onlinelibrary.wiley.com/doi/10.1002/adom.202301508 by City Universitaet Of Hong Kong, Wiley Online Library on [10/12/2023]. See the Terms and Conditions (https://onlinelibrary.wiley.com/terms-and-conditions) on Wiley Online Library for rules of use; OA articles are governed by the applicable Creative Commons License

drain-source electrodes with asymmetric electrical contact area. The asymmetric carrier diffusion caused by the designed asymmetric electrical contact area enables a different electric field intensity in the channel near the drain and the source electrodes, resulting in the asymmetric photocurrent under global illumination. Therefore, the device can achieve an admiring photoresponse at zero bias. The photoresponse mechanism of the device was further systematically investigated by scanning photocurrent mapping (SPCM) and Kelvin probe force microscope (KPFM). Finally, at zero bias, the device exhibits a low dark current of ≈1 nA, ultrahigh photocurrent/dark current ratio of 1.57×10^4, high specific detectivity (D^*) of 3.24×10^9 Jones, and relatively fast response speed of ≈720 µs at room temperature. Our findings demonstrate that the straightforward electrode contact area design strategy offers a workable concept for creating a high-performance infrared photodetector operating at room temperature.

4. Experimental Section

Growth of Te Nanobelts: High-quality Te nanosheets/nanobelts were prepared via a modified CVD method, where TeO_2 powder was used as the precursor.[19] A single-zone tubular furnace equipped with a quartz tube was used as the reaction chamber. In a typical reaction, 30 mg TeO_2 powder (99.999%, Sigma–Aldrich) loaded into a ceramic boat was placed at the center of the single zone tube furnace, and mica (1 cm × 1 cm) as the deposition substrate was placed at the downstream end of the tube around 10 cm outside the heating zone. Before the reaction, the tube was pumped to 8×10^{-3} Torr first and then refilled with 10% H_2/Ar gas mixture for three times to remove residual oxygen. During the reaction, 100 sccm gas mixture of Ar and H_2 (the volume ratio of H_2 is 10%) was introduced both as the carrier gas and reductive agent. The furnace temperature was programmed to gradually increase to the target temperature (≈600–800 °C) in 40 min and then maintained for 20 min. After that, the furnace was cooled down in the atmosphere of 100 sccm Ar gas until room temperature.

Device Fabrication and Characterization: The electrodes on 300 nm SiO_2/p^{++}-Si substrates were defined via electron beam lithography (EBL) (VEGA3, TESCAN) followed by the thermal evaporation of metal. The synthesized Te samples were transferred onto the electrodes and substrates by a dry transfer technique. The morphology and surface potential of the fabricated device were measured by AFM and KPFM (Bruker Dimension Icon), respectively. Raman spectra and scanning photocurrent mapping were measured by a high-resolution confocal Raman microscope (WITec Alfa-300) under the excitation of a 532 nm laser at room temperature. The channel current evolution of the device was monitored at ambient condition by a semiconductor parameter analyzer (Agilent 4155C). The lasers used for photodetection were purchased from Changchun New Industries Optoelectronics Technology in China. The response speed was characterized by connecting the device to a preamplifier (SR570, Stanford) and a digital oscilloscope (TBS 1102B-EDU, Tektronix). The laser was modulated by an arbitrary function generator (AFG-2005, Gw Instek). The spectra of current noise power density of Te devices were measured by a semiconductor parameter analyzer (PX600, Platform Design Automation, Inc.).

Supporting Information

Supporting Information is available from the Wiley Online Library or from the author.

Acknowledgements

H.W. and H.H. contributed equally to this work. This work was supported by the State Key Research Development Program of China (Grant No. 2019YFB2203503 and YS2022YFB3200011), China Postdoctoral Science Foundation (2021M702242 and 2022T150431), National Natural Science Foundation of China (62105211 and U21A20511), Science and Technology Innovation Leading Talents Program of Guangdong Province (No. 2019TX05C343), Department of Education of Guangdong Province (No. 2022ZDZX1023), Basic and Applied Basic Research Foundation of Guangdong Province-Regional Joint Fund-Key Projects (2022B1515120012 and 2019B1515120043), Central Military Commission Science and Technology Committee Project (2022-JCJQ-JJ-0886), Science and Technology Innovation Commission of Shenzhen (JCYJ20200109105608771 and KCXFZ20211020163814021), Key Projects (B) of the Stability Support Program for Shenzhen Higher Education Institutions (No. 20220810151419001), Natural Science Foundation of Sichuan Province (2022NSFSC1800), Project supported by State Key Laboratory of Luminescence and Applications (SKLA-2020-03), National Taipei University of Technology-Shenzhen University Joint Research Program (2021008), Natural Science Foundation of Jiangsu Province (BK20210076), and Natural Science Foundation of Jiangsu Higher Education Institutions of China (19KJB470035). C.T. thanks the funding support from the National Natural Science Foundation of China – Excellent Young Scientists Fund (Hong Kong and Macau) (52122002) and ECS scheme (21201821) from the Research Grant Council of Hong Kong.

Conflict of Interest

The authors declare no conflict of interest.

Data Availability Statement

The data that support the findings of this study are available from the corresponding author upon reasonable request.

Keywords

asymmetric electrical contact, high sensitivity, infrared photodetectors, low dark current, tellurium

Received: June 30, 2023
Revised: September 5, 2023
Published online: October 22, 2023

[1] W. Gawron, P. Martyniuk, A. Keblowski, K. Kolwas, D. Stepien, J. Piotrowski, P. Madejczyk, M. Pedzinska, A. Rogalski, *Solid-State Electron.* **2016**, *118*, 61.
[2] C. Liu, J. Guo, L. Yu, J. Li, M. Zhang, H. Li, Y. Shi, D. Dai, *Light- Sci. Appl.* **2021**, *10*, 123.
[3] X. Guan, X. Yu, D. Periyanagounder, M. R. Benzigar, J.-K. Huang, C.-H. Lin, J. Kim, S. Singh, L. Hu, G. Liu, D. Li, J.-H. He, F. Yan, Q. J. Wang, T. Wu, *Adv. Opt. Mater.* **2021**, *9*, 2001708.
[4] J. Zha, M. Luo, M. Ye, T. Ahmed, X. Yu, D.-H. Lien, Q. He, D. Lei, J. C. Ho, J. Bullock, K. B. Crozier, C. Tan, *Adv. Funct. Mater.* **2022**, *32*, 2111970.
[5] M. Peng, Z. Wen, X. Sun, *Adv. Funct. Mater.* **2022**, *33*, 2211548.
[6] N. Youngblood, C. Chen, S. J. Koester, M. Li, *Nat. Photonics* **2015**, *9*, 247.
[7] F. Xia, T. Mueller, Y.-M. Lin, A. Valdes-Garcia, P. Avouris, *Nat. Nanotechnol.* **2009**, *4*, 839.
[8] W. Liu, J. Lv, L. Peng, H. Guo, C. Liu, Y. Liu, W. Li, L. Li, L. Liu, P. Wang, S. C. Bodepudi, K. Shehzad, G. Hu, K. Liu, Z. Sun, T. Hasan, Y. Xu, X. Wang, C. Gao, B. Yu, X. Duan, *Nat. Electron.* **2022**, *5*, 281.

© 2023 The Authors. Advanced Optical Materials published by Wiley-VCH GmbH

21951071, 2023, 23, Downloaded from https://onlinelibrary.wiley.com/doi/10.1002/adom.202301508 by City Universitaet Of Hong Kong, Wiley Online Library on [10/12/2023]. See the Terms and Conditions (https://onlinelibrary.wiley.com/terms-and-conditions) on Wiley Online Library for rules of use; OA articles are governed by the applicable Creative Commons License

[9] Q. Guo, A. Pospischil, M. Bhuiyan, H. Jiang, H. Tian, D. Farmer, B. Deng, C. Li, S.-J. Han, H. Wang, Q. Xia, T.-P. Ma, T. Mueller, F. Xia, *Nano Lett.* **2016**, *16*, 4648.
[10] M. Amani, C. Tan, G. Zhang, C. Zhao, J. Bullock, X. Song, H. Kim, V. R. Shrestha, Y. Gao, K. B. Crozier, M. Scott, A. Javey, *ACS Nano* **2018**, *12*, 7253.
[11] L. Tong, X. Huang, P. Wang, L. Ye, M. Peng, L. An, Q. Sun, Y. Zhang, G. Yang, Z. Li, F. Zhong, F. Wang, Y. Wang, M. Motlag, W. Wu, G. J. Cheng, W. Hu, *Nat. Commun.* **2020**, *11*, 2308.
[12] Y. Wang, Z. Yu, Y. Tong, B. Sun, Z. Zhang, J.-B. Xu, X. Sun, H. K. Tsang, *Appl. Phys. Lett.* **2020**, *116*, 211101.
[13] N. Sefidmooye Azar, J. Bullock, V. R. Shrestha, S. Balendhran, W. Yan, H. Kim, A. Javey, K. B. Crozier, *ACS Nano* **2021**, *15*, 6573.
[14] A. D. Oyedele, S. Yang, L. Liang, A. A. Puretzky, K. Wang, J. Zhang, P. Yu, P. R. Pudasaini, A. W. Ghosh, Z. Liu, C. M. Rouleau, B. G. Sumpter, M. F. Chisholm, W. Zhou, P. D. Rack, D. B. Geohegan, K. Xiao, *J. Am. Chem. Soc.* **2017**, *139*, 14090.
[15] Q. Liang, Q. Wang, Q. Zhang, J. Wei, S. X. Lim, R. Zhu, J. Hu, W. Wei, C. Lee, C. Sow, W. Zhang, A. T. S. Wee, *Adv. Mater.* **2019**, *31*, 1807609.
[16] J. Wu, H. Ma, C. Zhong, M. Wei, C. Sun, Y. Ye, Y. Xu, B. Tang, Y. Luo, B. Sun, J. Jian, H. Dai, H. Lin, L. Li, *Nano Lett.* **2022**, *22*, 6816.
[17] Y. Wang, G. Qiu, R. Wang, S. Huang, Q. Wang, Y. Liu, Y. Du, W. A. Goddard, M. J. Kim, X. Xu, P. D. Ye, W. Wu, *Nat. Electron.* **2018**, *1*, 228.
[18] Z. Shi, R. Cao, K. Khan, A. Tareen, X. Liu, W. Liang, Y. Zhang, C. Ma, Z. Guo, X. Luo, H. Zhang, *Nano-Micro Lett.* **2020**, *12*, 99.
[19] P. Yang, J. Zha, G. Gao, L. Zheng, H. Huang, Y. Xia, S. Xu, T. Xiong, Z. Zhang, Z. Yang, Y. Chen, D.-K. Ki, J. J. Liou, W. Liao, C. Tan, *Nano-Micro Lett.* **2022**, *14*, 109.
[20] M. Xu, J. Xu, L. Luo, M. Wu, B. Tang, L. Li, Q. Lu, W. Li, H. Ying, L. Zheng, H. Wu, Q. Li, H. Jiang, J. Di, W. Zhao, Z. Zhang, Y. He, X. Zheng, X. Gan, Z. Liu, X. Wang, W. Huang, *Mater. Today* **2023**, *63*, 50.
[21] J. Li, J. Zhang, J. Chu, L. Yang, X. Zhao, Y. Zhang, T. Liu, Y. Lu, C. Chen, X. Hou, L. Fang, Y. Xu, J. Wang, K. Zhang, *Iscience* **2023**, *26*, 106177.
[22] C. Zhao, C. Tan, D.-H. Lien, X. Song, M. Amani, M. Hettick, H. Y. Y. Nyein, Z. Yuan, L. Li, M. C. Scott, A. Javey, *Nat. Nanotechnol.* **2020**, *15*, 53.
[23] J. Zha, S. Shi, A. Chaturvedi, H. Huang, P. Yang, Y. Yao, S. Li, Y. Xia, Z. Zhang, W. Wang, H. Wang, S. Wang, Z. Yuan, Z. Yang, Q. He, H. Tai, E. H. T. Teo, H. Yu, J. C. Ho, Z. Wang, H. Zhang, C. Tan, *Adv. Mater.* **2023**, *35*, 2211598.
[24] C. Shen, Y. Liu, J. Wu, C. Xu, D. Cui, Z. Li, Q. Liu, Y. Li, Y. Wang, X. Cao, H. Kumazoe, F. Shimojo, A. Krishnamoorthy, R. K. Kalia, A. Nakano, P. D. Vashishta, M. R. Amer, A. N. Abbas, H. Wang, W. Wu, C. Zhou, *ACS Nano* **2019**, *14*, 303.
[25] C. Tan, M. Amani, C. Zhao, M. Hettick, X. Song, D. Lien, H. Li, M. Yeh, V. Shrestha, K. Crozier, M. Scott, A. Javey, *Adv. Mater.* **2020**, *32*, 2001329.
[26] H. Huang, J. Zha, S. Li, C. Tan, *Chin. Chem. Lett.* **2022**, *33*, 163.
[27] Z. Dong, W. Yu, L. Zhang, H. Mu, L. Xie, J. Li, Y. Zhang, L. Huang, X. He, L. Wang, S. Lin, K. Zhang, *ACS Nano* **2021**, *15*, 20403.
[28] L. Ye, H. Li, Z. Chen, J. Xu, *ACS Photonics* **2016**, *3*, 692.
[29] J. Yao, F. Chen, J. Li, J. Du, D. Wu, Y. Tian, C. Zhang, J. Yang, X. Li, P. Lin, *J. Mater. Chem. C* **2021**, *9*, 13123.
[30] R. Tian, X. Gan, C. Li, X. Chen, S. Hu, L. Gu, D. V. Thourhout, A. Castellanos-Gomez, Z. Sun, J. Zhao, *Light- Sci. Appl.* **2022**, *11*, 101.
[31] H. Wang, Z. Li, D. Li, X. Xu, P. Chen, L. Pi, X. Zhou, T. Zhai, *Adv. Funct. Mater.* **2021**, *31*, 2106105.
[32] P. Luo, F. Wang, J. Qu, K. Liu, X. Hu, K. Liu, T. Zhai, *Adv. Funct. Mater.* **2021**, *31*, 2008351.
[33] W. Wang, Y. Meng, W. Wang, Z. Zhang, P. Xie, Z. Lai, X. Bu, Y. Li, C. Liu, Z. Yang, S. Yip, J. C. Ho, *Adv. Funct. Mater.* **2022**, *32*, 2203003.
[34] X. Wang, P. Wang, J. Wang, W. Hu, X. Zhou, N. Guo, H. Huang, S. Sun, H. Shen, T. Lin, M. Tang, L. Liao, A. Jiang, J. Sun, X. Meng, X. Chen, W. Lu, J. Chu, *Adv. Mater.* **2015**, *27*, 6575.
[35] H. J. Jin, C. Park, K. J. Lee, G. H. Shin, S.-Y. Choi, *Adv. Mater. Technol.* **2021**, *6*, 2100494.
[36] D. Zheng, X. Dong, J. Lu, Y. Niu, H. Wang, *Small* **2022**, *18*, 2105188.
[37] Y. Chen, Y. Wang, Z. Wang, Y. Gu, Y. Ye, X. Chai, J. Ye, Y. Chen, R. Xie, Y. Zhou, Z. Hu, Q. Li, L. Zhang, F. Wang, P. Wang, J. Miao, J. Wang, X. Chen, W. Lu, P. Zhou, W. Hu, *Nat. Electron.* **2021**, *4*, 357.
[38] T. Mueller, F. Xia, P. Avouris, *Nat. Photonics* **2010**, *4*, 297.
[39] Z. Kang, Y. Cheng, Z. Zheng, F. Cheng, Z. Chen, L. Li, X. Tan, L. Xiong, T. Zhai, Y. Gao, *Nano-Micro Lett.* **2019**, *11*, 34.
[40] J. Kim, A. Venkatesan, N. A. N. Phan, Y. Kim, H. Kim, D. Whang, G.-H. Kim, *Adv. Electron. Mater.* **2022**, *8*, 2100941.
[41] M. Dai, C. Wang, M. Ye, S. Zhu, S. Han, F. Sun, W. Chen, Y. Jin, Y. Chua, Q. J. Wang, *ACS Nano* **2022**, *16*, 295.
[42] C. Zhou, S. Zhang, Z. Lv, Z. Ma, C. Yu, Z. Feng, M. Chan, *npj 2D Mater. Appl.* **2020**, *4*, 46.
[43] X. Zhang, M. Dai, W. Deng, Y. Zhang, Q. J. Wang, *Nanophotonics* **2023**, *12*, 607.
[44] C. Zhou, S. Raju, B. Li, M. Chan, Y. Chai, C. Y. Yang, *Adv. Funct. Mater.* **2018**, *28*, 1802954.
[45] F. Liu, Y. Yan, D. Miao, J. Xu, J. Shi, X. Gan, Y. Cheng, X. Luo, *Appl. Surf. Sci.* **2023**, *616*, 156444.
[46] M. Peng, Y. Yu, Z. Wang, X. Fu, Y. Gu, Y. Wang, K. Zhang, Z. Zhang, M. Huang, Z. Cui, F. Zhong, P. Wu, J. Ye, T. Xu, Q. Li, P. Wang, F. Yue, F. Wu, J. Dai, C. Chen, W. Hu, *ACS Photonics* **2022**, *9*, 1775.
[47] M. Peng, R. Xie, Z. Wang, P. Wang, F. Wang, H. Ge, Y. Wang, F. Zhong, P. Wu, J. Ye, Q. Li, L. Zhang, X. Ge, Y. Ye, Y. Lei, W. Jiang, Z. Hu, F. Wu, X. Zhou, J. Miao, J. Wang, H. Yan, C. Shan, J. Dai, C. Chen, X. Chen, W. Lu, W. Hu, *Sci. Adv.* **2021**, *7*, eabf7358.
[48] R. Frisenda, E. Navarro-Moratalla, P. Gant, D. Pérez De Lara, P. Jarillo-Herrero, R. V. Gorbachev, A. Castellanos-Gomez, *Chem. Soc. Rev.* **2018**, *47*, 53.
[49] S.-J. Yang, S. Choi, F. O. Odongo Ngome, K.-J. Kim, S. Y. Choi, C.-J. Kim, *Nano Lett.* **2019**, *19*, 3590.
[50] S. Fan, Q. A. Vu, M. D. Tran, S. Adhikari, Y. H. Lee, *2D Mater.* **2020**, *7*, 022005.
[51] S. Larentis, B. Fallahazad, E. Tutuc, *Appl. Phys. Lett.* **2012**, *101*, 223104.
[52] H. Wang, Y. Zeng, F. Meng, R. Cao, Y. Liu, Z. Guo, T. Wang, H. Hu, S. Fan, Y. Yang, S. Wageh, O. Al-Hartomy, A. Kalam, Y. Shao, Y. Zeng, D. Fan, H. Zhang, *Nano. Res.* **2023**, *16*, 10537.
[53] F. Wang, Z. Wang, K. Xu, F. Wang, Q. Wang, Y. Huang, L. Yin, J. He, *Nano Lett.* **2015**, *15*, 7558.
[54] H. Wang, S. Gao, F. Zhang, F. Meng, Z. Guo, R. Cao, Y. Zeng, J. Zhao, S. Chen, H. Hu, Y. Zeng, S. Kim, D. Fan, H. Zhang, P. Prasad, *Adv. Sci.* **2021**, *8*, 2100503.
[55] W. Wang, W. Wang, Y. Meng, Q. Quan, Z. Lai, D. Li, P. Xie, S. Yip, X. Kang, X. Bu, D. Chen, C. Liu, J. C. Ho, *ACS Nano* **2022**, *16*, 11036.
[56] C. Zhao, H. Batiz, B. Yasar, H. Kim, W. Ji, M. C. Scott, D. C. Chrzan, A. Javey, *Adv. Mater.* **2021**, *33*, 2100860.

© 2023 The Authors. Advanced Optical Materials published by Wiley-VCH GmbH

21951071, 2023, 23, Downloaded from https://onlinelibrary.wiley.com/doi/10.1002/adom.202301508 by City Universitaet Of Hong Kong, Wiley Online Library on [10/12/2023]. See the Terms and Conditions (https://onlinelibrary.wiley.com/terms-and-conditions) on Wiley Online Library for rules of use; OA articles are governed by the applicable Creative Commons License